Journal of Biomedical Optics 6(2), 214–223 (April 2001)

Pulsed photothermal radiometry as a method for investigating blood vessel-like structures

Christoph H. Schmitz
Uwe Oberheide
Stefan Lohmann
Holger Lubatschowski
Laser Zentrum Hannover e. V.
Hollerithallee 8
30419 Hannover, Germany

Wolfgang Ertmer
Institut für Quantenoptik der Universität Hannover,
Welfengarten 1
30167 Hannover, Germany

Abstract. Pulsed photothermal radiometry (PPTR) is known to be suitable for *in vivo* investigations of tissue optical properties. As a noncontact, nondestructive method it is a very attractive candidate for on-line dosimetry of laser treatments that rely on thermal laser–tissue interaction. In this article, we extend the one-dimensional (1D) analytical formalism that has widely been used to describe PPTR signals to a two-dimensional treatment of a simplified model of a blood vessel. This approach leads to quantitative description of a PPTR signal that, unlike in an 1D treatment, not only shows changes in time, but also varies in space. Using this approach, we are able to gain instructive understanding on how target characteristics of a blood vessel-like structure influence such a spatiotemporal PPTR signal. Likewise, the ability of extracting target features from those measurements is evaluated. Subsequently, we present experimental realization of the idealized model of a blood vessel as used in our theory. Comparison of actual PPTR measurements with theoretical predictions allow vessel localization laterally and in depth. Using our setup, we furthermore demonstrate the influence of flow inside the vessel on the measured signal.
[DOI: 10.1117/1.1344193]

Keywords: pulsed photothermal radiometry; blood vessels; on-line-dosimetry; tissue optics; thermal imaging; blood flow.

Paper JBO-90001 received Jan. 8, 1999; revised manuscript received Nov. 14, 2000; accepted for publication Nov. 27, 2000.

1 Introduction

Although the medical use of lasers has led to a vast variety of new therapeutic approaches, many of these applications are still unsatisfactory from a clinical point of view. Because laser-tissue interaction often occurs on a time scale too short for manual reaction, the process is difficult to control. Furthermore, a view of the treating process is often hidden by products of the treatment or the tissue itself.

The interactions are, in general, strongly dependent on tissue optical properties. Therefore, it is of great interest to determine and monitor the optical properties and their changes directly during treatment. Successful monitoring would allow one to control the dosimetry and hence improve most laser therapies.

We used pulsed photothermal radiometry (PPTR) for spectroscopic and structural investigations of tissue-like media. This method is based on time-resolved detection of thermal radiation that is emitted by a sample after irradiating it with a pulsed light source.[1]

This nondestructive noncontact approach, which has its origin in material testing,[2–4] shows attractive medical applications especially in dermatology. PPTR cannot only be used for determining optical properties of homogeneous samples[5] but also for detecting and localizing morphological substructures. This makes it a very promising tool for noninvasive investigations of pathological alterations, especially port wine stain (PWS) lesions.[6,7]

In many cases, PWS is modeled by one-dimensional layered structures.[8,9] Because this is an oversimplification in which many morphological features of these lesions are omitted, a growing number of higher dimensional approaches were investigated. They include Monte Carlo simulations of light transport in blood vessel-like geometries and numerical evaluations of heat transport phenomena for those structures.[10,11] Recently, two-dimensional (2D) thermal images were interpreted, yielding volumetric information about positions of blood vessels.[12] This was achieved using numerical inversion of the discretized solution of the PPTR formalism.

In this work we present a different approach of describing PPTR signals as produced by a single small blood vessel in a more or less homogeneous background medium. We restrict the structure investigated to a simplified geometry of a cylindrical vessel containing pure absorber in a transparent environment. Although this is an oversimplification, we favor this approach because it yields a closed-formula expression of the PPTR signal. Not only does this lead to a fast numerical evaluation it also provides an instructive understanding of the process of signal generation and the principal relations between target characteristics and signal features.

To strengthen the usefulness of our 2D model we present *in vitro* realization of this geometry in which actual measure-

Address all correspondence to Christoph H. Schmitz, SUNY Downstate Medical Center at Brooklyn, Box 25, 450 Clarkson Ave., Brooklyn, NY 11238. E-mail: cschmitz@downstate.edu

1083-3668/2001/$15.00 © 2001 SPIE

ments have been performed. We demonstrate determination of the lateral position and depth of a vessel-like structure in compliance with our model.

We also used this setup for an experimental demonstration of the changes in the PPTR signal due to flow of the absorber inside the vessel.

2 Theory

2.1 Model

Detailed theoretical treatments of PPTR signals for various applications and sample geometries have been presented in the past by several authors, see, e.g., Refs. 13 and 14. In the following, we summarize the most important results and develop a formalism that we adopted to describe our special geometry.

A pulsed photothermal signal is generated by transient heating of the target using a laser pulse and the subsequent thermal relaxation due to heat diffusion. Because we are dealing with watery samples/soft tissue this can be described by the heat conduction equation for thermal isotropic and homogeneous media. The temperature field $T(\mathbf{r},t)$ inside the sample in three dimensions is therefore given by

$$\frac{\partial T(\mathbf{r},t)}{\partial t} - \kappa \nabla^2 T(\mathbf{r},t) = 0, \tag{1}$$

with κ being the heat diffusion constant.

The initial condition for our problem is given by the temperature distribution due to the absorbed laser pulse energy,

$$T_0(\mathbf{r}) = T(\mathbf{r},0) = \frac{\mu_a(\mathbf{r}) E(\mathbf{r})}{\rho c}. \tag{2}$$

Here, $\mu_a(\mathbf{r})$, ρ, and c are the space dependent optical absorption coefficient of the target, its specific density, and specific heat, respectively; $E(\mathbf{r})$ is the spatial fluence.

A solution of Eq. (1) using the source term, Eq. (2), can be given when boundary conditions are applied. In the following, the sample geometry is described using Cartesian coordinates with the z axis running collinearly with the laser beam. We consider the heat loss to the ambient across the sample surface, lying in the plane $z=0$, to be negligible. This leads to a simple yet realistic boundary condition of an insulated surface, which can easily be treated using the method of Green's functions,[15]

$$T(\mathbf{r},t) = \frac{1}{8(\pi\kappa t)^{3/2}} \int_{V_0} dV' T_0(\mathbf{r}') \times \exp\left[-\frac{(x-x')^2 + (y-y')^2}{4\kappa t} \right] \times \exp\left[-\frac{(z-z')^2}{4\kappa t} + \exp - \frac{(z+z')^2}{4\kappa t} \right]. \tag{3}$$

In order to calculate the PPTR signal from this temperature field, we make two further assumptions: First, we assume perfect absorption of thermal radiation inside the sample. Instead of having to weigh contributions to the signal from all sample depths, this results in considering only the surface temperature.

This assumption is frequently used and is justified when focusing on samples with high water content (such as soft tissue) and detecting wavelengths, which are heavily absorbed in water. This condition is certainly fulfilled in our case because the detection method used (see Sec. 3) has its peak sensitivity around 13 μm where the absorption coefficient for water is $\sim 3000\ \mathrm{cm}^{-1}$.[16] This detection band has been chosen to match the wavelength of peak intensity of thermal radiation expected in our experiments.

A second common simplification is the use of a linearized form of the Stefan–Boltzmann law of radiation, where the intensity of thermal radiation is assumed to change proportionally with variations in temperature. This is a good approximation if the variation in temperature is small compared to the mean absolute temperature, which in our experiments is around 300 K. This condition is fulfilled because the laser-induced temperature changes have to be kept low (<10 K) in order not to induce thermal damage to the target.[17]

The measured PPTR signal amplitude $U(x,y,t)$ can then be modeled to be proportional to the surface temperature,

$$U(x,y,t) = K\, T(x,y,z=0,t). \tag{4}$$

Here, K is a scaling factor composed of various physical constants and a calibration factor, which amounts for the efficiency of the setup used, depending upon experimental details such as the detector surface, sensitivity, and the design of detection optics.

Using Eqs. (2) and (3) in Eq. (4), one obtains the following equation:

$$U(x,y,t) = K \frac{\mu_a}{4\rho c (\pi\kappa t)^{3/2}} \int_{V_0} dV'\, E(\mathbf{r}') \times \exp\left[-\frac{(x-x')^2 + (y-y')^2}{4\kappa t} \right] \exp\left(-\frac{z'^2}{4\kappa t} \right), \tag{5}$$

which is the convolution of the laser-generated heat source term with the thermal point spread function for the given boundary conditions. It sums up the contributions that every point of the heat source makes to the change in surface temperature at a given location. This makes clear the time dependence of the PPTR signal on the spatial distribution of the heat source, which in turn depends on the optical properties of the sample.

The solution of Eq. (5) can be interpreted as a two-dimensional time-dependent PPTR image, which depends on the spatial variation of the fluence $E(\mathbf{r}')$. We would like to point out that the model is not restricted to a particular spatial fluence distribution, and that thus far no assumptions about the optical properties of the target have been made.

Because we are interested in modeling PPTR signals generated by blood vessel-like structures, we restrict our investigations to a simplified geometry in which the blood vessel is represented by a purely absorbing cylinder embedded in a clear environment running parallel to the surface. This sample geometry is sketched in Figure 1. The beam diameter of the

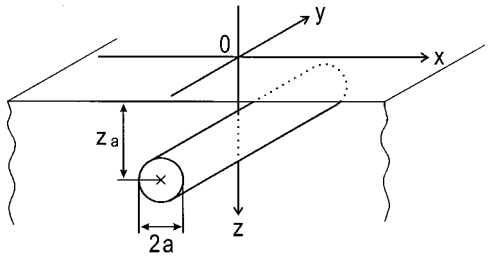

Fig. 1 Geometry and nomenclature for the model of a blood vessel.

laser is assumed to be broad compared to the vessel diameter, with a constant fluence value E_0 along x. The resulting initial temperature profile can be written

$$T_0(x',z')=\begin{cases}\dfrac{\mu_a E_0}{\rho c}\exp[-\mu_a(z'-z_a+\sqrt{a^2-x'^2})] \\ \qquad \text{for}\sqrt{x'^2+(z'-z_a)^2}\leqslant a, \\ 0 \quad \text{else,}\end{cases} \tag{6}$$

with μ_a and a being the absorption coefficient of the vessel and its radius, respectively, and z_a being the distance between the sample surface and vessel center. Figure 2 shows the light distribution inside the sample and illustrates the generation of a PPTR signal by a vessel-like structure.

The PPTR signal generated by this initial temperature distribution can be calculated using Eqs. (6) in Eqs. (3) and (4). Because the source term, Eq. (6), is independent of y, the volume integral in Eq. (3) can be evaluated in the y direction, leading to a factor of $2\sqrt{\pi\kappa t}$. The PPTR signal is then given by

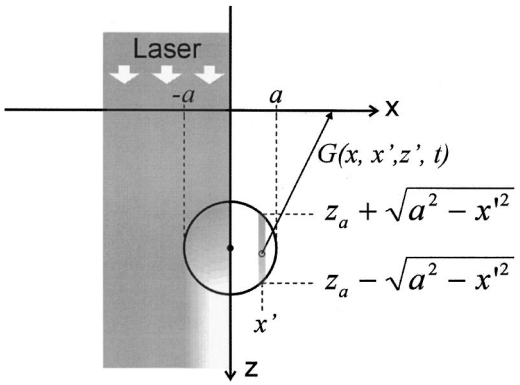

Fig. 2 Schematic diagram of irradiation and PPTR signal generation for the idealized geometry of a blood vessel. The part of the sketch on the left of the z axis side shows the light distribution inside the sample. Fluence values are shown by a gray scale with darker shading representing larger values. The right half of the sketch shows how a point (x',z') located inside the vessel contributes to the surface temperature $T(x,t)$. This can formally be expressed by the Green's function $G(x,x',z',t)$. Also depicted are the limits of integration.

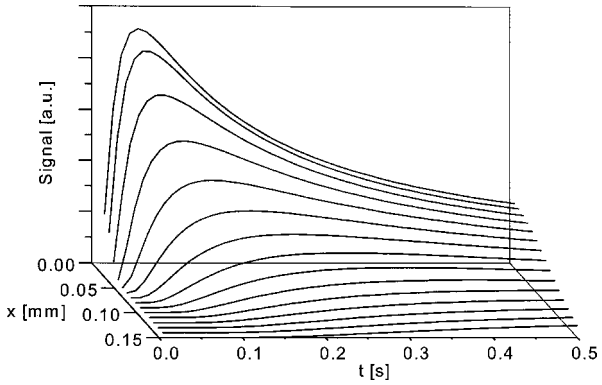

Fig. 3 Pseudo-3D plot of simulated PPTR signals at various distances x from the vessel. Sample parameters used: $z_a=200\,\mu$m, $a=90\,\mu$m, and $\mu_a=120\,\text{cm}^{-1}$. The calculations are based on Eq. (7).

$$U(x,t)=K\frac{E_0\mu_a}{2\pi\rho c\kappa t}\int_{-a}^{a}dx'\int_{z_a-\sqrt{a^2-x'^2}}^{z_a+\sqrt{a^2-x'^2}} \times\exp[-\mu_a(z'-z_a+\sqrt{a^2-x'^2})] \times\exp\left[-\frac{(x-x')^2+z'^2}{4\kappa t}\right]dz'. \tag{7}$$

The result, Eq. (7), is the basis of all calculations throughout the following discussions. It mimics the absorption-dominated light propagation inside a blood vessel and the relatively weak contributions to the PPTR signal from the surrounding dermis.

In all of the foregoing considerations, the sample is regarded to be thermally homogeneous. Because of the high water content of soft tissue and the use of water-based phantoms, we approximate the thermal properties of the target in all calculations with those of water: $\kappa=0.001\,43\,\text{cm}^2\,\text{s}^{-1}$, $\rho=1\,\text{g}\,\text{cm}^{-3}$, $c=4.182\,\text{J}\,\text{K}^{-1}\,\text{g}^{-1}$.[18]

2.2 Simulation Studies

To illustrate the characteristics of the PPTR signal obtained on our model, Figure 3 shows a pseudo-three-dimensional (3D) plot of the numerical evaluation of Eq. (7) for a typical set of sample properties. The vertical axis represents the amplitude value of the PPTR signal at a certain location and time. The x-axis value corresponds to the position at which the signal is evaluated and represents the lateral distance from the vessel. The time axis corresponds to the time elapsed after applying the light pulse. Hence, each of the curves shown represents the amplitude of a PPTR signal versus time for a position x on the sample surface. Every curve shows a characteristic ''peak'' or signal maximum that occurs, delayed, after the initial light pulse. Both the amplitude and delay of the peak vary depending on position x. Directly above the vessel $(x=0)$, the peak amplitude assumes its maximum and shows the shortest delay.

Although always qualitative of this shape, the quantitative signal form strongly depends on the particular target properties, the reason why the method provides dosimetric information. In the following we investigate the influence of the target properties on distinct signal features. For example, one would expect the delay time of the signal peak to increase with in-

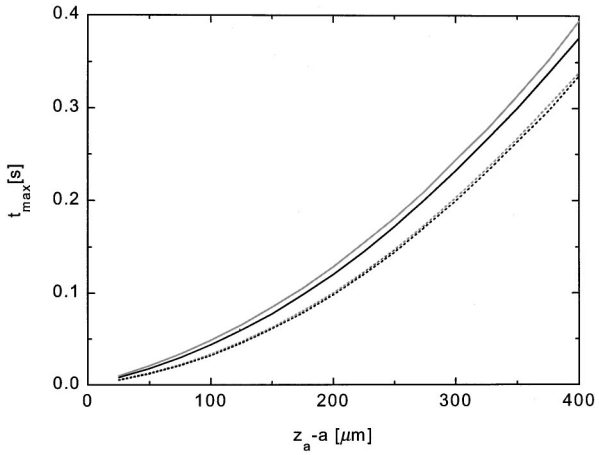

Fig. 4 Signal simulations based on Eq. (7) showing the delay time t_{max} of the signal peak at location $x=0$ dependent on the vessel depth. Parameters: Vessel radius: $a=45\ \mu$m (- - -), $a=90\ \mu$m (—); vessel absorption: $\mu_a=60\ \text{cm}^{-1}$ (gray), and $\mu_a=120\ \text{cm}^{-1}$ (black).

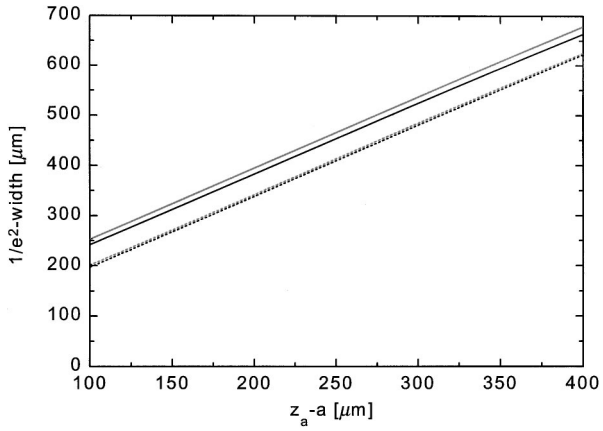

Fig. 5 Signal simulations based on Eq. (7) showing the width of the temperature profile ($1/e^2$ width of the Gaussian fit) at t_{max} vs vessel depth. Parameters: Vessel radius: $a=45\ \mu$m (- - -), $a=90\ \mu$m (—); vessel absorption: $\mu_a=60\ \text{cm}^{-1}$ (gray), and $\mu_a=120\ \text{cm}^{-1}$ (black).

creasing vessel depth. We test if such considerations can provide a relatively simple means of extracting target features by systematically investigating the influence of changes in target properties on the following specific signal features:

- the delay time of the signal peak (referred to as t_{max}),
- the lateral width of the signal at t_{max},
- the signal peak amplitude $U(0, t_{max})$.

In the following, we show numerical evaluations of Eq. (7) and discuss the dependence of those signal features on varying vessel properties absorption coefficient μ_a, radius a, and depth z_a-a.

Figure 4 shows the dependence of the delay time t_{max} of the signal peak at $x=0$ on the vessel depth for varying vessel sizes and absorption coefficients. Because the depth of the vessels determines the distance of heat diffusion to the surface, t_{max} increases with larger vessel depth. For a spatiotemporal point heat source (i.e., the Green's function), it is easy to show by differentiation that the time at which the temperature assumes its maximum at a given distance L varies proportionally to L^2. Because in our model, the signal results from convolution of the Green's function with a complex source term, a strict quadratic dependence of t_{max} on the vessel depth cannot be expected.

Furthermore, the graph shows growth of t_{max} with increasing capillary diameter and decreasing absorption coefficient. The first effect is due to the fact that the vessel forms a volume heat source. Therefore, a larger diameter leads to contributions to the surface temperature change from increased distances, thereby effectively increasing the time at which the signal maximum occurs.

The influence of the vessel absorption results from the difference between depositing the optical energy in a small (larger μ_a) or in a large volume (smaller μ_a). In the first case, the mean heat diffusion length is shorter, therefore leading to an earlier signal maximum.

In our simulations, we furthermore investigated the spatial width of the temperature profile along the x axis, depending on the sample properties. We therefore applied Gaussian fits to a cross section of the profile at t_{max} [$U(x, t_{max})$] and used the e^2 width as a measure of width. One Gaussian proved to fit the profiles very well in all cases. This is not surprising, since $U(x,t)$ is a convolution of a strongly located source term with a Gaussian diffusion term. Therefore, $U(x,t)$ is not *exactly* of Gaussian shape, but very similar to it. The profile gets closer to being Gaussian with increasing distance x and for longer times t. The dependence of the e^2 width of $U(x, t_{max})$ on the vessel depth, absorption, and radius is plotted in Figure 5.

The width increases linearly with growing vessel depth. This is because heat diffusion occurs isotropically in every direction, thus causing the isothermal front to spread spatially. The relationship between a wider profile for larger vessels is clear. The influence of vessel absorption lies again in the effect of creating a small volume source for strong absorption and a larger volume source for weaker absorption, the latter causing a net increase of the mean diffusion length. As before, this effect becomes stronger with increasing vessel diameter.

The third discrete signal feature whose dependence on sample properties was theoretically investigated using Eq. (7) is the signal peak amplitude $U(x=0, t_{max})$.

Figure 6 shows a strongly decreasing signal with increasing vessel depth. As one would expect, thick capillaries produce higher signals than thin ones. Strongly absorbing vessels result in consistently higher signal amplitude because this leads to a reduced mean diffusion distance.

Figures 4–6 show how distinct signal features are influenced by certain properties of our vessel model. In principle, the measurement of those distinct features could be used to determine target properties that have an important impact on dosimetry. This might be a more feasible alternative to fitting 3D datasets to measured surface maps of the temperature distribution.

However, from looking at the modeled data it is clear, that the unambiguous determination of target properties from simple signal features is not easily accomplished. For instance, the influence of investigated vessel properties is qualitatively similar on both the peak delay t_{max} and the width

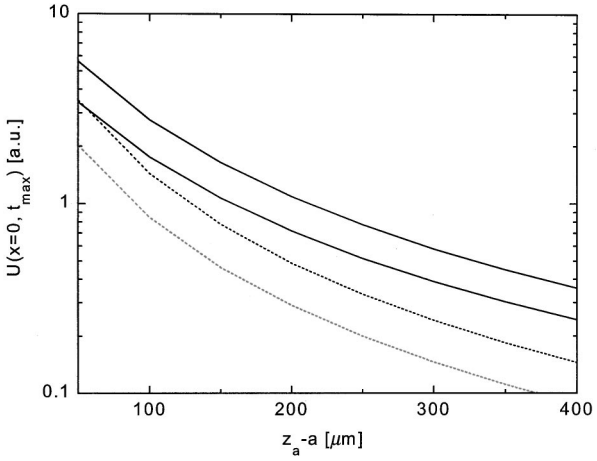

Fig. 6 Signal simulations based on Eq. (7) showing the amplitude of the signal peak $U(0,t_{max})$ vs vessel depth. Parameters: Vessel radius: $a=45\ \mu$m (- - -), $a=90\ \mu$m (—); vessel absorption: $\mu_a=60\ \text{cm}^{-1}$ (gray), and $\mu_a=120\ \text{cm}^{-1}$ (black).

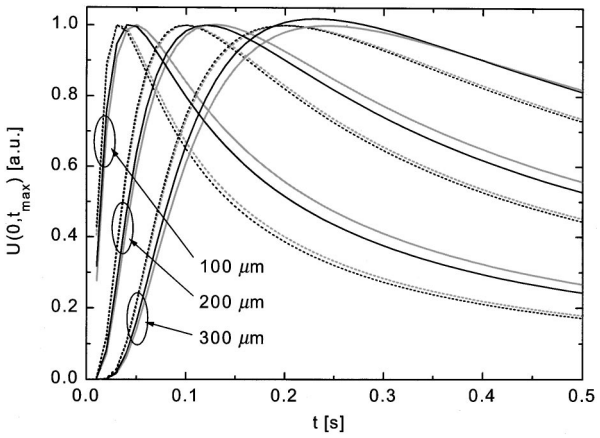

Fig. 7 Simulated time dependent PPTR signals $U(0,t)$ for various vessel depths. Parameters: Vessel radius: $a=45\ \mu$m (- - -), $a=90\ \mu$m (–); vessel absorption: $\mu_a=60\ \text{cm}^{-1}$ (gray), and $\mu_a=120\ \text{cm}^{-1}$ (black).

of the temperature profile. The situation can be improved by using the amplitude information investigated in Figure 6. This measurement shows a strong and qualitatively different dependence on the target parameters. Like all absolute methods, this measurement requires system calibration, i.e., the comparison of a measured signal to a known reference. Because of the calibration uncertainties, problems due to drift, and instabilities in the setup, it is much more difficult to provide an absolute amplitude measurement with good accuracy than measuring, e.g., the spatial width of a temperature profile. We are also aware of the additional problem of noise corruption in measured signals.

We nevertheless believe the theoretical signal considerations above to be very valuable for understanding the process of signal generation. It is also appreciated that a scenario with fewer free target parameters improves the situation. For example, the absorption coefficient of blood at the used laser wavelength is known.

Using Eq. (7), we further simulated the influence of target properties of a vessel geometry on the temporal shape of a PPTR signal $U(0,t)$. Figure 7 shows some simulated curves. The shape of the curves is qualitatively similar to experiments on one-dimensional (1D)-layered media.[8,9] The difference is the use of a medium showing 2D structures and performing the measurement in one surface point (or line) above the vessel. All signals have been normalized to one. Every set of sample parameters produces an individual signal form. This demonstrates that it is principally possible to extract vessel parameters such as absorption, size, and depth from simple (nonscanning) PPTR measurements on such structures.

3 Materials and Methods

A typical PPTR setup is shown in Figure 8. As a pulsed light source we used a free running Nd:YLF laser with a pulse duration of 150 μs at a wavelength of 1052 nm. This system is easy to handle and offers good performance, such as high pulse energy (up to 240 mJ) and small pulse energy variations ($<5\%$). The repetition rate is variable between 0.2 and 20 Hz. For irradiating the sample we used a quartz/quartz multimode fiber of 1.2 mm core diameter and 0.22 numerical aperture (NA) with a nonspherical outcoupling lens. This provides a maximum of flexibility and a uniform beam profile. The radiant exposure in all experiments was kept below $200\ \text{mJ/cm}^2$.

The infrared detector is a liquid nitrogen cooled photoconductive HgCdTe type with a peak detectivity of $3.3\times10^{10}\ \text{cm Hz}^{1/2}\ \text{W}^{-1}$ at a wavelength of 13 μm (EG&G Judson model J15D16-M204-S02M-60) and a cutoff-wavelength of 16 μm. The detection area of $2\times2\ \text{mm}^2$ is imaged onto the sample surface by means of an $f=35$ mm ZnSe lens. The size of the detection spot can be varied from $\sim1\ \text{mm}^2$ to $\sim1\ \text{cm}^2$. A 7 μm long-pass filter is used to block stray light, resulting in an effective detection bandwidth of 7–16 μm.

Reflecting the thermal radiation with a gold mirror and irradiating the sample from above allows the use of liquid phantoms. Avoiding the use of gel-like media such as gelatine or agar gel offers an easier and more flexible way of producing phantoms. Furthermore, the thermo-optical properties are easier to control and are more stable.[19]

Figure 9 shows a schematic drawing of an *in vitro* model of a blood vessel that we developed for the studies presented. The blood vessel is mimicked by a glass capillary with an inner diameter of 180 μm and a wall thickness of 10 μm, which is embedded in an ambient fluid. The capillary is mounted parallel to the ground of a cuvette ($\sim8\ \text{cm}\times10\ \text{cm}$

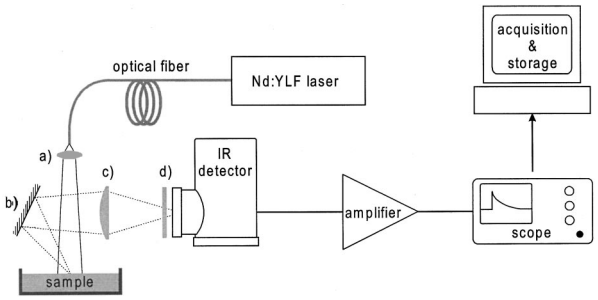

Fig. 8 Schematic diagram of the experimental setup. (a) Fiber collimator; (b) gold mirror; (c) ZnSe lens; (d) long-pass filter.

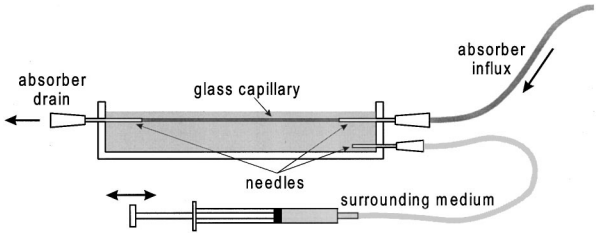

Fig. 9 Cross section of the *in vitro* model of a blood vessel. A glass capillary is mounted parallel to the bottom of a cuvette containing the ambient medium. Syringes are used to control the liquid level in the cuvette and to fill the capillary.

$\times 2$ cm inner dimensions) and is attached to two injection needles acting as influx and drain. The capillary can be filled with fluid by means of a syringe, which is connected to the influx needle by a small hose. This setup allows the use of liquids of desired optical and thermal properties for both the background medium and the vessel. In our experiment, both were filled with watery agents with thermal properties that are basically that of water ($\kappa = 0.001\,43\,\mathrm{cm^2\,s^{-1}}$, $\rho = 1\,\mathrm{g\,cm^{-3}}$, $c = 4.182\,\mathrm{J\,K^{-1}\,g^{-1}}$)[18] and therefore similar to those of soft tissue. We consider the phantom as thermally homogeneous and neglect the weak influence of the capillary wall.

Besides its flexibility in realizing various optical constitutions, the main advantage of the concept described is the possibility of easy yet accurate vessel depth adjustment. This is achieved by altering the volume of the surrounding medium and thus its level above the capillary. A volume change of 1 mL background medium amounts to a 125 μm change in capillary depth.

In order to create the environment described by our theoretical model, the cuvette was filled with pure water, whose absorption at the excitation wavelength (1052 nm) is very low ($\sim 0.36\,\mathrm{cm^{-1}}$) and therefore can be neglected over the relevant optical path.[16]

The capillary was filled with a mixture of 2% black India ink (Rotring® TT 17) in water, yielding an absorption coefficient of $\mu_a = 120\,\mathrm{cm^{-1}}$ at the excitation wavelength. This value had been separately confirmed in our lab with standard transmission measurements and quantitative 1D-PPTR measurements. Although we are aware of possible effects of light scattering, these measurements indicate that light propagation in the ink is strongly dominated by absorption and that it can be accurately described by Beer's law. Therefore, we neglected effects of light scattering in our model.

In the following, we describe two principal setups of our experiment that we used to assess our 2D phantom.

Figure 10 shows details of the PPTR setup that was used to demonstrate the lateral localization of a vessel. A relatively large surface area of a few $\mathrm{mm^2}$ is probed by the detector while scanning a focused laser beam across the sample surface. The detection spot remains at a fixed position with respect to the target. This setup is not compliant with the geometry of our theoretical model because 2D treatment is not possible for a focused, scanning laser beam. It does therefore not allow any quantitative evaluation.

Figure 11 shows another setup for spatial resolved PPTR measurements which is compliant with the geometry of our two-dimensional formalism.

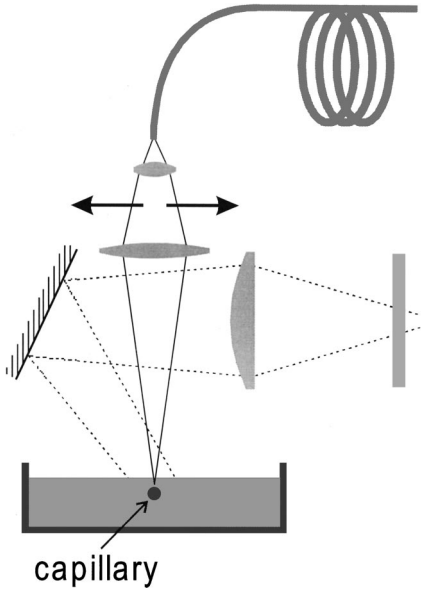

Fig. 10 Details of the experimental setup for localizing the vessel-like structure by focusing and scanning the laser beam over a broad detection area.

In this example, the sample is irradiated with a broad laser beam (0.8 cm diameter), and point-like detection is performed at various locations on the surface. In our setup, this can be achieved by scanning the focused spot of the detector across the sample surface. A more convenient alternative would be the use of a fast pixel detector (thermocamera).

Although, from a theoretical standpoint, the setup in Figure 11 would be the design of choice, its realization suffers from a few practical limitations. Considering the simulations shown in Figure 3, spatial variations in the surface temperature on a 100 μm scale can be expected. The detection spot

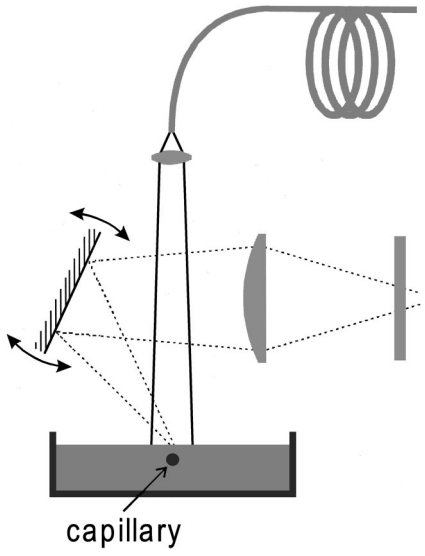

Fig. 11 Details of the experimental setup for spatially resolved PPTR measurements. Spatial resolution is achieved by scanning the detection spot, e.g., by tilting the mirror.

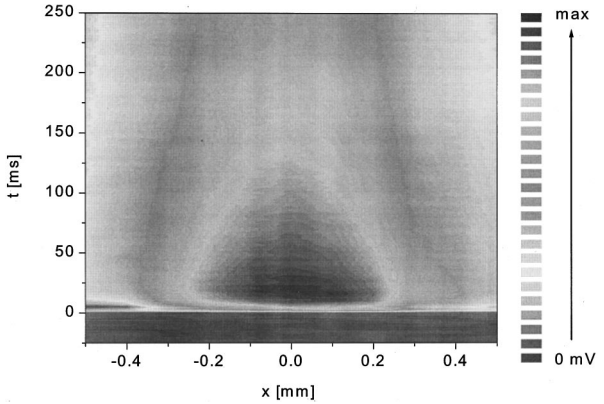

Fig. 12 Gray scale map of the temporally and spatially varying PPTR signal amplitude obtained from the *in vitro* blood vessel model according to the setup in Figure 10. The *x* axis shows the lateral position of the laser with respect to the vessel.

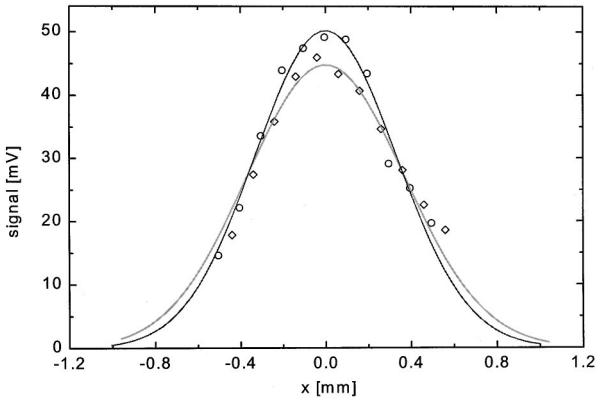

Fig. 13 Signal amplitude at t_{max} vs lateral position of the laser spot x. Signals of a superficial capillary and appropriate Gaussian fit (dark gray circles); signals and fit (light gray diamonds) of a capillary of 10 μm additional depth.

has to be smaller than this ($\sim$ several tens of μm) to be able to resolve such structures.

In order to optimize the signal to noise level of our experiment, detection of thermal radiation is performed over a wide wavelength range. To reduce Fresnel losses and for reasons of design simplicity and cost, we use simple detection optics consisting of a single lens. This leads to strong chromatic aberration and hence difficulties in focusing the detector to a sufficiently small spot. In our experiment, the chromatic variation of the refractive index over the wavelength range detected ($\sim 7-16\,\mu$m) causes a change of the focal length between $f_{7\,\mu m} = 34.6$ mm and $f_{16\,\mu m} = 36.6$ mm. The smallest detection spot possible with our detection optics is on the order of 1 mm^2. Therefore, with our setup we are not able to laterally obtain varying PPTR data of spatial resolution that would be sufficient to be evaluated using Eq. (7).

However, we can make use of the formalism developed in Sec. 2 if we restrict the number of free parameters. This will be demonstrated further in Sec. 4.2.

4 Experimental Results

In the following, we present the results that can be obtained with the two principal setups discussed and shown in Figures 10 and 11 in Sec. 3.

We focus on two main topics: first, lateral localization of the vessel and, second, determination of the vessel depth. Additionally, photothermal detection of absorber flow inside a capillary will be demonstrated.

4.1 Lateral Localization of the Vessel

Figure 12 shows the spatially resolved PPTR signal obtained from the *in vitro* blood vessel model with the setup in Figure 10. The results are presented as a nonlinear encoded gray scale map of the signal's amplitude in order to achieve better representation of the data.

The image is composed of 11 single PPTR measurements, which have been recorded at a fixed detection location with the illumination spot moving in steps of 0.1 mm along the *x* axis, i.e., perpendicular to the capillary (see the geometry in Figure 1). Due to the laser that was available and the delivery optics used, the minimum laser spot size achievable was slightly less than 1 mm in diameter. Because the beam profile is not a flat top but rather of rounded shape, no abrupt appearance of a PPTR signal occurs when scanning the laser across the sample.

Because the amplitude is plotted versus one temporal and one spatial axis, the graph is in a form similar to a streak camera image. The glass capillary can be localized easily due to the intensity maximum around $x = 0$ at every time t.

A more detailed discussion is possible by looking at the cross sections of the gray scale plot. In Figure 13 the signal is plotted versus the laser's x position for the time at which the signal's maximum occurs (~ 10 ms). Two sets of data are shown: one for the measurement shown in Figure 12 and one for a capillary of additional 10 μm depth. For the sake of clarity, Gaussian fits are shown for both data sets.

The full widths at half maximum (FWHMs) of the fits are 0.4 and 0.5 mm for the more superficial and the deeper lying vessel, respectively. This is two to three times the actual vessel diameter and still of the order of the structure's dimension. Because of the well-localized centers of the fits, we believe a vessel to be laterally localizable within an uncertainty of a few tens of μm.

The depth of the more superficial capillary was of the order of 50 μm but has not been determined exactly because no independent measuring tools (e.g., ultrasound, optical coherence tomography, etc.) were available. A relative change in depth is easily accomplished by adding a known volume to the background medium in the cuvette. A detailed discussion of the influence of the capillary depth on the measured signals is given in Sec. 4.2.

4.2 Determination of Vessel Depth

Figure 14 shows measured signals obtained using the setup shown in Figure 10 with the laser irradiation set to $x = 0$, i.e., directly at the vessel. The curves represent different depths of the capillary, each varying by 25 μm.

The topmost curve was taken at the minimum depth of the capillary of a few tens of μm. This distance to the surface had to be kept in order to not affect its smoothness due to adhesive forces, which would disturb the measurement. Although the

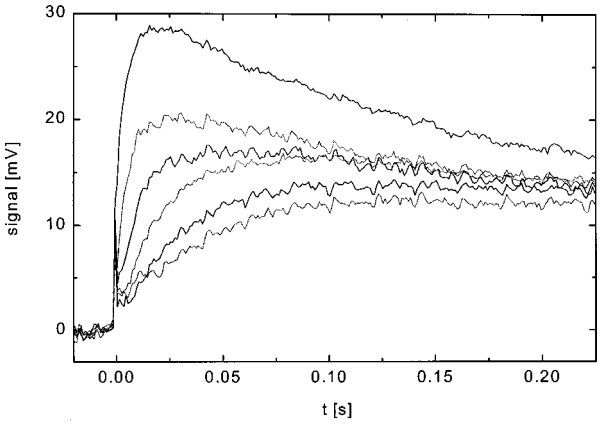

Fig. 14 Signals obtained for the laser spot at $x=0$. Different curves correspond to different capillary depths, increasing for the curves from top to bottom by 25 μm.

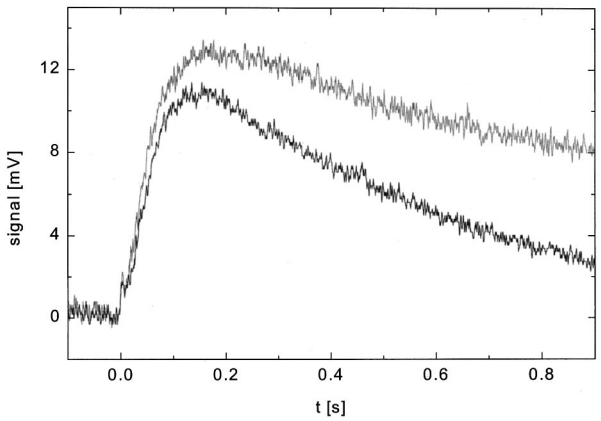

Fig. 16 Comparison of PPTR signals obtained on a vessel-like structure at rest (gray) and with a flowing (black) absorber.

level of the liquid environment can be controlled accurately, allowing precise alteration of the vessel depth, the absolute depth is hard to determine on a 10 μm scale (see above).

As can be seen in Figure 14, the curves can be distinguished clearly, thus allowing separation of the vessels, which vary in depth by a few tens of μm. Because a focused laser spot was used, the condition for a two-dimensional treatment is not fulfilled, and therefore a signal description according to Sec. 2.1 cannot be given.

Quantitative depth determination can be made if a slightly different setup is used. The signal shown in Figure 15 was recorded under conditions of both broad irradiation (0.8 cm diameter) and detection, which again complies with the two-dimensional geometry assumed in Sec. 2.2. In the case of a sufficiently large detection spot size, the signal can be modeled by integrating Eq. (7) along the x axis. As a practical matter, numerical evaluation of the integral along x in Eq. (7) is performed over a range that is sufficiently larger than the width of a significant temperature increase, say, several mm.

Three calculated curves are shown in comparison, representing capillary depths of $z_a - a = 170$, 180, and 190 μm. The other sample parameters were known to be $a = 90\,\mu$m and $\mu_a = 120\,\mathrm{cm}^{-1}$. Because we did not perform a calibrated measurement, all curves were scaled to the PPTR signal's maximum. The curves calculated can easily be distinguished by their rise time and shape of decay. Although the PPTR signal shows significant noise, the calculation for a depth of 180 μm is clearly identified as showing the best fit. Taking this result into consideration, we believe our method allows depth determination within an uncertainty of $< \pm 6\%$.

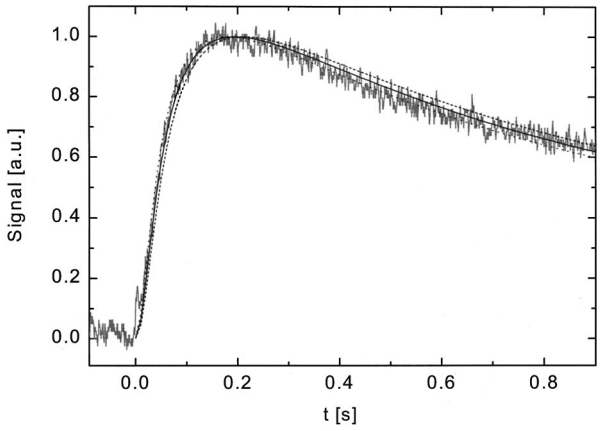

Fig. 15 Signal (gray) recorded under conditions according to two-dimensional formalism. Calculated signals for various capillary depths of 170 (···), 180 (—), and 190 μm (- - -).

4.3 Influence of Absorber Flow

In the following, we demonstrate the detection of absorber flow in a blood vessel-like structure by means of a PPTR measurement. For that purpose, the phantom was modified in such a way that a reservoir containing absorber at a filling level above the capillary could be connected to it.

Changing the filling level in the reservoir and therefore the hydrostatic pressure allows the absorbing liquid to flow through the blood vessel model at the desired speed. The average flow velocity can easily be determined by measuring the volume change over time and taking into account the capillary diameter. Using a relatively large reservoir and keeping the change in the liquid level small during the duration of the experiment results in negligible variation in pressure and flow velocity.

We chose a rate of $3.9\,\mathrm{cm\,s}^{-1}$, a typical flow velocity in blood vessels of approximately the diameter we used in our model.[20] Measurements were performed with both broad irradiation and detection. The vessel volume probed was roughly 0.2 μL.

The results are shown in Figure 16. The signal plotted in gray is the same as that in Figure 15, taken at a capillary depth of 140 μm and the absorber at rest. The other signal (black) is obtained with the same sample configuration but with the absorber flowing at a constant rate of $3.9\,\mathrm{cm\,s}^{-1}$.

As can also be seen in Figure 16, the absorber flow gives rise to reduced amplitude, a slightly earlier signal maximum, and steeper decay. These effects can qualitatively be understood with regard to additional convective heat transfer and thereby resulting heat loss inside the sample volume of interest.

5 Discussion

In this work, we investigated the theoretical and experimental aspects of using PPTR as a tool for on-line diagnostics on blood vessel-like structures. This is desired mainly in dermatological laser treatments but also provides new aspects of on-line control in microsurgery. For the sake of an easy and fast way in which to calculate formalism a simplified model of such morphological structures has been developed.

We furthermore presented the *in vitro* model of a 180 μm diameter blood vessel that allows wide adjustment of parameters such as vessel depth, optical properties, and even control over the flow velocity inside the vessel.

The photothermal signals calculated were discussed with regard to their spatial and temporal behavior, and showed distinct features that characteristically depend on various model properties. We investigated the influence of vessel size, depth, and absorption. Although some of these properties influence the signal in a similar manner and therefore are hard to distinguish, the simulations suggest that they can be separated when full signal information (amplitude, spatiotemporal shape) is taken into account.

Initial measurements on our phantom show the PPTR signals to vary significantly with displacements of a vessel-like structure, both laterally and in depth.

The PPTR image obtained by scanning a detector perpendicularly to a superficial vessel coarsely reproduces the vessel dimension and allows its lateral localization within a few tens of μm. Because of experimental restrictions, mainly those due to the low spatial resolution of our detection system, a full quantitative evaluation of spatially varying PPTR signals obtained on such structures has yet to be performed.

However, we demonstrated our formalism to be applicable to quantitative analysis of a simplified experimental setup involving a 2D target.

For various vessel depths at given vessel sizes and absorption, we were able to clearly identify a best fitting curve showing excellent agreement within the $\sim$5% noise [root mean square (rms)] of the signal. This is an uncertainty in depth determination of less than 6% of the 180 μm depth of the vessel-like structure. Because only an integrated measurement could be performed, thereby giving up information about the lateral shape of the temperature profile, and because of the lack of signal amplitude calibration, we were able to extract only one out of three free vessel parameters. However, because of the distinct signatures of the signals modeled in Figure 7, we are confident that a high-spatial resolution PPTR signal and a more rigorous analysis would allow the simultaneous extraction of more target features with similar accuracy.

Nevertheless we do believe that our simplified approach of a reduced set of free parameters might have useful practical applications. For example, the absorption coefficient of blood vessels can be estimated beforehand. This suggests also the use of our method together with other techniques that are capable of adding information about the target.

In order to realize this, further improvements of the experiment are necessary. Most important is increased spatial detection resolution. Options include the use of a single-element scanning detector with improved focusing optics and a thermocamera. In the case of using a scanning system, imaging quality might greatly be improved using reflective optics, which avoid problems of chromatic aberration.

A further perspective of experimental improvement is the realization of more complex optical properties. The case of added background absorption can be implemented in the analytical treatment shown in this article. Using light scattering suspensions of known optical properties, the effect of light scattering can be studied as well. However, our simple absorption-based theory does not apply to this case of light transport so a more sophisticated signal description would have to be implemented.

In most cases of modeling PPTR signals, the bioheat equation is reduced to a pure heat conduction equation omitting convective components.[11,21] Because effects of convection might affect the dosimetry especially in dermatological applications on superficial blood vessels, we also investigated the influence of the movement of the absorber inside the vessel model. For that reason, signals were recorded with a constant flow of absorbing medium inside the model vessel.

Because PPTR signals on tissue typically decay on a time scale of the order of tenths of a second, even absorber flow at rates as low as a few cm s^{-1} could clearly be detected. For the vessel size used, this amounts to volumetric flow on the order of μL/s.

On one hand, we believe this to be an important indication for taking convection quantitatively into account in photothermal dosimetry. On the other hand, this demonstration suggests the application of PPTR for on-line controlling the success in coagulating a blood vessel or testing the vitality of tissue. It is worth noting that the method is not restricted to a regime of negligible light scattering in the background medium.

We are aware that the tissue phantom shown does not resemble the arbitrary geometry that blood vessels can assume. Nevertheless, we consider it a very useful ''zero-order'' approach for studying the feasibility of PPTR measurements on isolated vessel-like structures. This includes static as well as dynamic phenomena under well-defined conditions.

PPTR is known to be a promising tool in diagnostics and on-line controlling. We believe it offers full performance in imaging morphological structures in more than one dimension.

In our work we demonstrated how morphological information can be extracted from a simplified two-dimensional model of a blood vessel if thermal imaging is performed and multidimensional analysis of the data is carried out.

References

1. S. O. Nordal and P. E. Kanstad, ''Photothermal radiometry,'' *Phys. Scr.* **20**, 659 (1979).
2. G. Busse, ''Optoacoustic and photothermal inspection techniques,'' *Appl. Opt.* **21**(1), 107 (1982).
3. W. P. Leung and A. C. Tam, ''Thermal conduction at a contact interface measured by pulsed photothermal radiometry,'' *J. Appl. Phys.* **63**(9), 1845 (1988).
4. R. E. Imhoff, B. Zhang, and D. J. S. Birch, ''Photothermal radiometry for non-destructive evaluation,'' in *Non Destructive Evaluation*, A. Mandelis, Ed., p. 186, Prentice Hall, Englewood Cliffs, NJ (1994).
5. S. A. Prahl, I. A. Vitkin, U. Bruggemann, B. C. Wilson, and R. R. Anderson, ''Determination of optical properties of turbid media using pulsed photothermal radiometry,'' *Phys. Med. Biol.* **37**(13), 1203 (1993).
6. J. S. Nelson, S. L. Jacques, and W. H. Wright, ''Determination of thermal and physical properties of port wine stain lesions using

pulsed photothermal radiometry,'' *Proc. SPIE* **1643**, 287 (1992).
7. S. L. Jacques, J. S. Nelson, W. H. Wright, and T. E. Milner, ''Pulsed photothermal radiometry of port wine stain lesions,'' *Appl. Opt.* **32**(13), 2439 (1993).
8. F. H. Long and T. H. Deutsch, ''Pulsed photothermal radiometry for depth profiling of layered media,'' *Appl. Phys. Lett.* **51**(25), 2076 (1987).
9. T. E. Milner, D. J. Smithies, D. M. Goodman, A. Lau, and J. S. Nelson, ''Depth determination of chromophores in human skin by pulsed photothermal radiometry,'' *Appl. Opt.* **35**(19), 3379 (1996).
10. W. Verkruysse, J. W. Pickering, J. F. Beek, M. Keijzer, and J. C. van Gemert, ''Modeling the effect of wavelength on the pulsed dye laser treatment of port wine stains,'' *Appl. Opt.* **32**(4), 939 (1993).
11. S. Gabay, G. W. Lucassen, W. Verkruysse, and M. J. C. van Gemert, ''Modeling the assessment of port wine stain parameters from skin surface temperature following a diagnostic laser pulse,'' *Lasers Surg. Med.* **20**, 179 (1997).
12. D. J. Smithies, T. E. Milner, and J. S. Nelson, ''Three dimensional tomographic reconstruction of simulated and *in vivo* sub-surface chromophores,'' *Proc. SPIE* **2975**, 14 (1997).
13. W. P. Leung and A. C. Tam, ''Techniques of flash radiometry,'' *J. Appl. Phys.* **56**(1), 153 (1984).
14. I. A. Vitkin, B. C. Wilson, and R. R. Anderson, ''Pulsed photothermal radiometry studies in tissue optics,'' in *Optical-Thermal Response of Laser-Irradiated Tissue*, A. J. Welch and M. J. C. van Gemert, Eds., p. 535, Plenum, New York (1995).
15. H. S. Carslaw and J. C. Jaeger, ''Conduction of heat in solids,'' 2nd ed., Clarendon, Oxford (1959).
16. G. M. Hale and M. R. Querry, ''Optical constants of water in the 200-nm to 200-μm wavelength region,'' *Appl. Opt.* **12**(3), 555 (1973).
17. J. Pearce and S. Thomsen, ''Rate process analysis of thermal damage,'' in Ref. 14, p. 561.
18. J. W. Valvano, ''Tissue thermal properties and perfusion'' in Ref. 14, p. 445.
19. C. H. Schmitz, T. Hantzko, S. Lohmann, H. Lubatschowski, and W. Ertmer, ''Pulsed photothermal radiometric investigations of optical and thermal properties,'' *Proc. SPIE* **2923**, 12 (1996).
20. R. F. Schmidt, *Physiologie des Menschen*, G. Thews, Ed., 23rd ed., p. 501, Springer, New York (1987).
21. J. Roider and R. Birngruber, ''Solution of the heat conduction equation,'' in Ref. 14, p. 385.